Available Online

J. Sci. Res. **17** (1), 57-70 (2025)

JOURNAL OF SCIENTIFIC RESEARCH

www.banglajol.info/index.php/JSR

rGO Blended PbS Nanoparticles for the Effective Degradation of Methylene Blue Dye and Growth Inhibition against *B. subtilis* Bacteria

C. Rajashree[1], A. R. Balu[1,*], M. Sriramraj[1], K. Devendran[1], A. Vinith[1], N. Arunkumar[1,2], V. Rajamani[1]

[1]Department of Physics, AVVM Sri Pushpam College (Affiliated to Bharathidasan University, Tiruchirappalli), Poondi, Tamilnadu, India

[2]Department of Physics, Anjalai Ammal-Mahalingam Engineering College (Affiliated to Anna University, Chennai), Kovilvenni, Tamilnadu, India

Received 15 April 2024, accepted in final revised form 9 October 2024

Abstract

A simple one-pot synthesis method was used to synthesize reduced graphene oxide (rGO) blended PbS nanocomposite (NC) from *Centella asiatica* leaf extract. Its photocatalytic and antibacterial properties were studied and compared with that of PbS nanoparticles (NPs) synthesized by precipitation method. PbS with cubic structure was confirmed by XRD studies. With the incorporation of rGO, the size of PbS crystals decreased from 27 nm to 23 nm. For rGO-blended PbS, grain boundaries are well defined and agglomeration is minimised. Pb–S related bands seem to shift towards lower wavenumber side for rGO-PbS NC. PL intensity decreased for rGO-PbS NC due to suppression of recombined photoelectrons and holes. With rGO inclusion, the absorption edge shifted towards higher wavelength, decreasing the band gap. By providing larger surface area, rGO enhanced the photodegradation efficiency of PbS from 84.38 % to 95.06 % against methylene blue (MB)under visible light. Bacterial growth inhibition nature of PbS improved with rGO incorporation.

Keywords: rGO; Precipitation; Organic dyes; Antibacterial.

doi: https://dx.doi.org/10.3329/jsr.v17i1.72669 J. Sci. Res. **17** (1), 57-70 (2025)

1. Introduction

Photovoltaic, photodetector, optoelectronics, and data storage are all benefits from semiconducting nanomaterials' outstanding physical and chemical properties [1]. Its tunable band gap (0.7 to 2.1 eV) and energy level modification make lead sulfide (PbS) an attractive semiconductor material for optoelectronic applications [2]. Besides these, PbS exhibits high absorption coefficient, quantum confinement, large Bohr radius, admirable mobility of carriers and multiple exciton generation [3]. PbS's characteristics has made it useful in the area of photography, lasers, sensors, photocatalysts, biological fields, thermoelectrics, etc. [4]. In addition to solar radiation converting devices, PbS can also be used to create photoelectrochemical cells [5]. As a result of the carrier confinements, PbS exhibits

[*]*Corresponding author*: arbalu757@gmail.com

exceptional nonlinear optical properties, which can also be used in optical devices [6]. Recently, PbS nanoparticles (NPs) based photodetectors have been reported to outperform conventional Indium Gallium Arsenide photodetectors [7]. Besides exhibiting significant structural, electrical and chemical properties, PbS possess stable crystal structure and mechanical stability which makes it useful for electrochemical charge storage and conversion in pseudocapacitors [8]. In spite of these applications, PbS exhibits several drawbacks affecting the efficiencies of PbS derived devices. Prominent dark current and longer response times limit its usage in photodetector devices [9]. Surface chemistry of PbS NPs, as well as passivation of their dangling bonds, are essential for efficient optoelectronic devices. As a result of surface oxidation and the formation of hydroxyl motifs, PbS' stability is greatly reduced when exposed to air [10]. To overcome the above demerit, PbS NPs used for fabricating these devices must be monodisperse, stable under atmospheric conditions, and capable of carrying photogenerated electron-hole pairs [11].

Nowadays, carbon related materials such as graphene, graphene oxide and reduced graphene oxide (rGO) has received high popularity in many research areas due to their high thermal and electrical conductivity, surface area, mechanical properties and good electrochemical stability [12]. Among the carbon based materials, rGO which is a derivative of graphene possesses high thermal conductivity, effective adsorption and greater surface area. Being an electron reservoir, recombination rate of charge carriers in rGO is minimized due to suitable path way for electron transfer [13]. rGO consists of small number of oxygen functional groups on its basal plane and at edges which can effectively help to attach the transition metal oxide/sulfide NPs as well as prevent them from agglomeration for better device performances. With these advantages, it is possible to address the issues related to pure PbS by forming composite with rGO. Recently, several research groups have demonstrated that rGO inclusion improves the device performances of metal oxide/sulfides [14-17]. In this work, rGO-blended PbS NPs were synthesized by reducing graphene oxide using *Centella asiatica* leaf extract by a facile one-pot synthesis method. Synthesized rGO-PbS nanocomposite (NC) was studied for its photocatalytic and antibacterial properties, and its results were compared with those for pure PbS.

2. Experimental Studies

The precursor salts used to synthesize PbS and rGO-blended PbS NPs are lead nitrate with 99.8 % purity, Rankhem Chemicals, India (0.1 M), thiourea with assay 99 %, Rankhem Chemicals, India (0.1 M) and graphene oxide powder purchased from Adnano Technologies, India (purity 98 %).

2.1. *Synthesis of PbS NPs*

To 135 mL de-ionized water, lead nitrate (4.968 g) and thiourea (1.142 g) were added and stirred well to which 15 mL liquid NH_3 was added to maintain the pH at 10. The resulting

solution was stirred for 4 h and kept undisturbed. Precipitates were found settled which were filtered, washed, calcined at 350 °C for 2 h and crushed to get PbS NPs.

2.2. *Preparation of C. asiatica leaf extract*

C. asiatica leaves were collected, washed, and boiled at 70 °C for 45 min with distilled water (30 mL). The resultant extract was stored at 4 °C for further experiments.

2.3 *rGO-PbS NC synthesis*

In 120 mL of de-ionized water, 3 mg of GO powder was added and treated ultrasonically for 45 min. Afterward, 30 mL of leaf extract and precursor salts (lead nitrate and thiourea) used for the synthesis of PbS NPs were added and stirred well for 2 h at 100 °C.The resultant was filtered, washed, calcined at 200 °C for 45 min and crushed to get rGO-PbS nanocomposite.

2.4. *Characterization*

The crystal structure was studied using X'pert PRO Analytical - PW 340/60 diffractometer (Malvern PANanalytical Ltd, India). Surface morphology was analyzed using HITACH S-3000 H scanning electron microscope (Hitachi, Japan). Functional group analysis was done using a FTIR spectrometer (RX-1, Perkin Elmer, Richmond Scientific Ltd, UK). Optical absorption studies were performed by a UV-visible spectrophotometer (LAMBDA 35, Perkin Elmer, India). Photoluminescnce spectra was obtained using variancary spectrometer (VARCaryECP-02, Agilent, USA).

2.5. *Photocatalytic test*

The photodegradation ability of PbS and rGO-PbS NPs were tested against methylene blue (MB) dye under visible light. In 10 mL dye solution, PbS and rGO-PbS catalysts (2 mg) were added and stirred in dark and light conditions. The catalysts were centrifuged and absorbance spectra were obtained at 460 nm after centrifuging 2 mL of dye at every equal interval of time (20 min).

2.6. *Antibacterial activity*

*Bacillus subtilis*bacterial growth inhibition of PbS NPs and rGO-PbS NCs was tested. Bacterial strain was allowed to grow on petri plates containing Muller-Hinton agar. In wells (6 mm) created, PbS and rGO-PbS NPs (6 mg) dissolved in dimethyl sulfoxide (DMSO) (20, 40, 60, 80 μL) were placed. Due to the resistance by the NPs, zones of inhibition was developed after an incubation period of 24 h at 37 °C from which the antibacterial activity was evaluated.

3. Results and Discussion

3.1. *X-ray diffraction (XRD) studies*

X-ray diffraction (XRD) analysis was performed to determine the crystal structure and purity of PbS and rGO-PbS NC. Fig. 1 shows the XRD patterns of PbS and rGO-PbS NC. Polycrystalline nature with peaks corresponding to (110), (200), (220), (311), (222), (400), (331), (420) and (422) planes were observed.

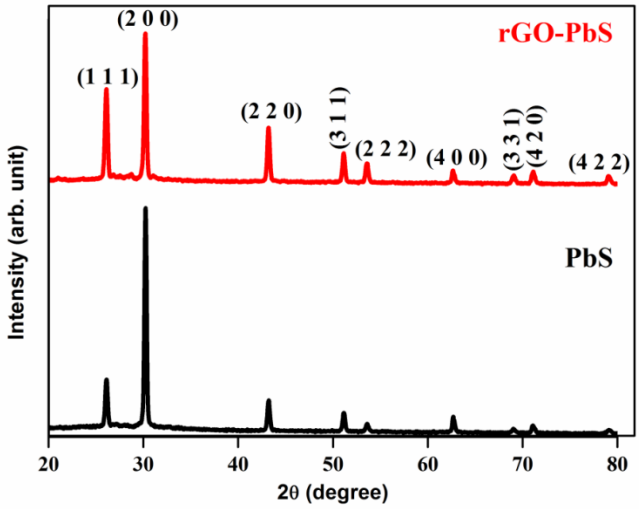

Fig. 1. XRD patterns of PbS and rGO-PbS.

PbS's cubic crystal structure (JCPDS Card 65-0692) fits all peaks well. For rGO-PbS, no diffraction peaks other than the characteristic ones of PbS was observed confirming the fact that the crystal structure of PbS is not affected with rGO inclusion [18]. rGO-PbS might not display peaks related to rGO due to the intercalation of PbS matrix into graphene sheets [19]. Also, the peak intensities of rGO-PbS was found lower than that of pure PbS due to graphene coating which supports the fact that rGO has been incorporated onto PbS matrix. Crystallite sizes calculated using Scherrer formula were 27 and 23 nm for PbS and rGO-PbS NC. A decrease in crystallite size for the rGO-PbS NC might be due to rGO-induced disruptions in PbS crystal nucleation [20].

3.2. *Scanning electron microscope (SEM) analysis*

Scanning electron microscope (SEM) analysis is a high-resolution imaging technique that uses a focused beam of electrons to examine the surface morphology of a sample. Fig. 2 shows the SEM images of PbS and rGO-PbS NC. Grains were found uniformly distributed.

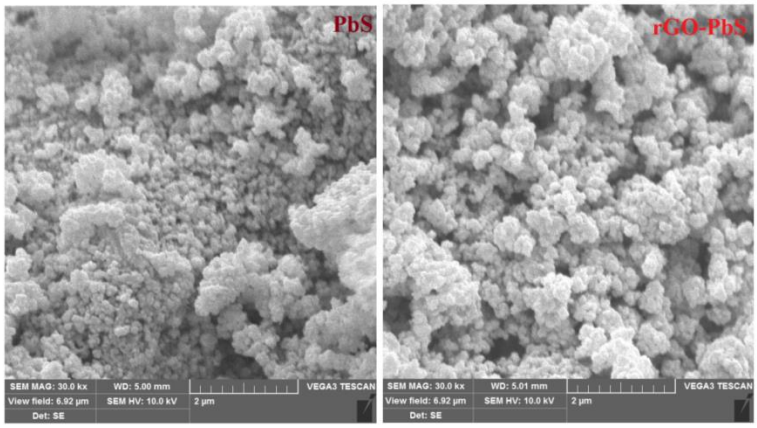

Fig. 2. SEM images of PbS NPs and rGO-PbS NC.

Irregular shaped grains with different sizes is observed for pure PbS nanoparticles. Grains appear to be agglomerated with few pinholes. rGO incorporation minimized the agglomeration, resulting in grains with well-defined boundaries for rGO-PbS composite.

3.3. *FTIR spectra*

FTIR spectra analysis was performed to determine the functional groups present in the tested samples. Fig. 3 shows the FTIR spectra of pure PbS and rGO-PbS NC. O–H stretchings occured at 3384, 1631 cm^{-1} for PbS and at 3504, 1620 cm^{-1} for rGO-PbS [21].

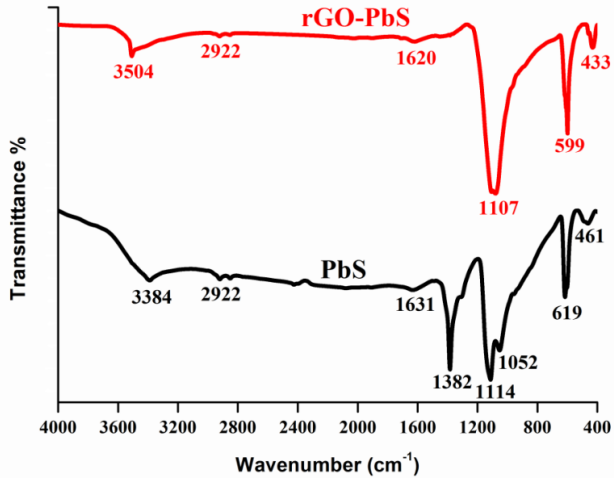

Fig. 3. FTIR spectra of PbS NPs and rGO-PbS's NC.

PbS exhibits a vibrational band at 1382 cm^{-1} due to molecular adsorption of atmospheric CO_2. SO_4 antisymmetric stretching occurs at 1114 for PbS and at 1107 cm^{-1} for

rGO-PbS [22]. C–C bonding occured at 1052 cm^{-1} for PbS. Peaks related to heteropolar diatomic molecule of PbS occured at 619, 461 for PbS and at 599, 433 cm^{-1} for rGO-PbS [23]. Particle size, dispersion states and strong interactions between PbS NPs and rGO sheets, can be attributed to the shift in the Pb-S band observed for the rGO-PbS NC [24].

3.4. *Photoluminescence (PL) studies*

Photoluminescence study is an effective non-destructive tool to evaluate the precise band edge emission, defects and transitions occurring in metal oxide/sulfide semiconductors. Fig. 4 shows the PL spectra of PbS and rGO-PbS NC. Near band edge emission peaks attributed to free exciton annihilation are observed at 364 nm for PbS and at 356 nm for rGO-PbS NC [25].

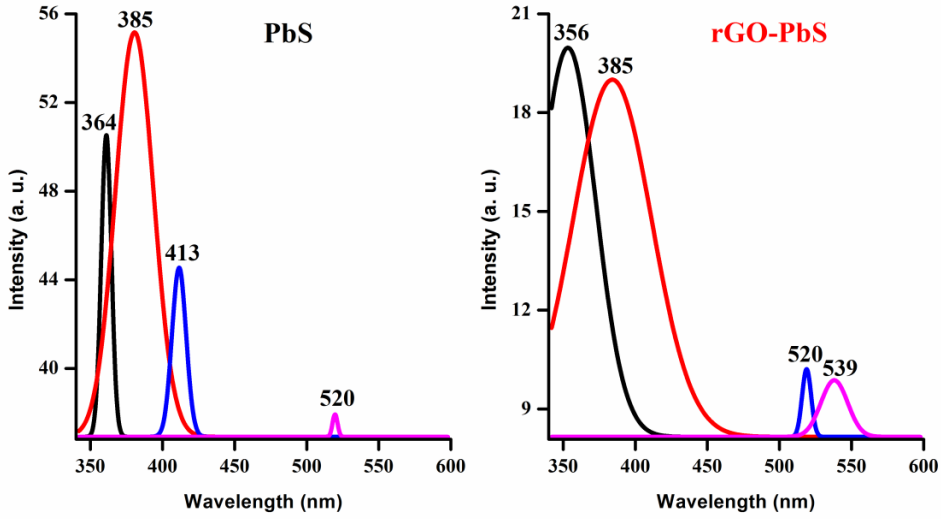

Fig. 4. PL spectra of PbS and rGO-PbS NC.

High energy excitonic emission due to quantum confinement occured at 385 nm for both PbS NPs and rGO-PbS NC [26]. Pristine PbS showed a peak at 413 nm because of an interstitial sulfur lattice defect [27]. As sulfur vacancy electrons trapped in the valence band recombined with holes, a 520 nm peak was emitted from both samples [28]. For the rGO-PbS NC, sulfur species may be responsible for the peak at 539 nm [29]. The rGO-PbS NC has reduced PL peak intensity compared to pure PbS. Suppression of recombined photoelectrons and holes are responsible for the decrease in luminescence intensity. The PL peak intensity indicates electrons/holes recombination rates; low PL peak intensity indicates low recombination, and vice versa [30].

3.5. *Optical studies*

In photocatalysis, the optical absorption properties of the photocatalyst play a significant role in the photodegradation of organic dyes. The optical absorption properties, including the band gap of PbS and rGO-PbS NC were estimated by UV-vis-diffuse reflectance spectroscopy in the range of 200-1000 nm. After introduction of rGO, PbS showed enhanced absorption due to light absorbing nature of rGO (Fig. 5a). Furthermore, PbS's absorption edge shifted towards higher wavelengths with rGO inclusion in favour of its lower band gap.

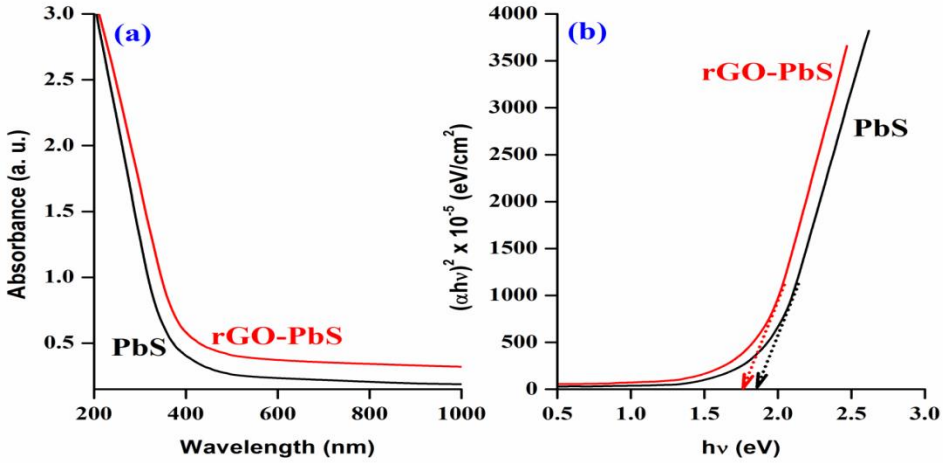

Fig. 5. (a) Absorbance spectra and (b) Tauc plots of PbS and rGO-PbS NC.

Similar red shift in absorption edge has been reported earlier for rGO activated NiO [31]. To calculate the band gap energies (E_g) of the PbS and rGO-PbS NC, Tauc equation ($h\nu = A\ (h\nu\text{-}E_g)^n$) is used, where *h* and *v* are Planck's constant and frequency, respectively. From Tauc plots (Fig. 5b) of PbS and rGO-PbS, the estimated E_g values are 1.85 and 1.76 eV, respectively. The decreased E_g value for the rGO-PbS NC might be due to charge delocalization from electronic interaction between PbS and rGO [32].

3.6. *Photocatalytic activity*

For evaluating the photocatalytic activity of PbS and rGO-PbS NC, MB dye was used as a model pollutant under visible light irradiation. When the photocatalytic reaction progresses the absorbance peak of MB at 460 nm decreased for both catalysts, but the rGO-PbS catalyst exhibited a better diminishing tendency (Fig. 6). A plot of C/C_0 versus reaction time was used to estimate the residual concentration of MB after degradation (Fig. 7). The equation used to estimate the decomposition efficiency (%) is:

$$\text{Decomposition efficiency (\%)} = \left(1 - \frac{C}{C_0}\right) \times 100 \quad (1)$$

where C_0 represents original concentration of MB under dark and C signifies the concentration after time 't'. rGO-PbS catalyst exhibited a maximum degradation efficiency of 95.06 % (Fig. 8).

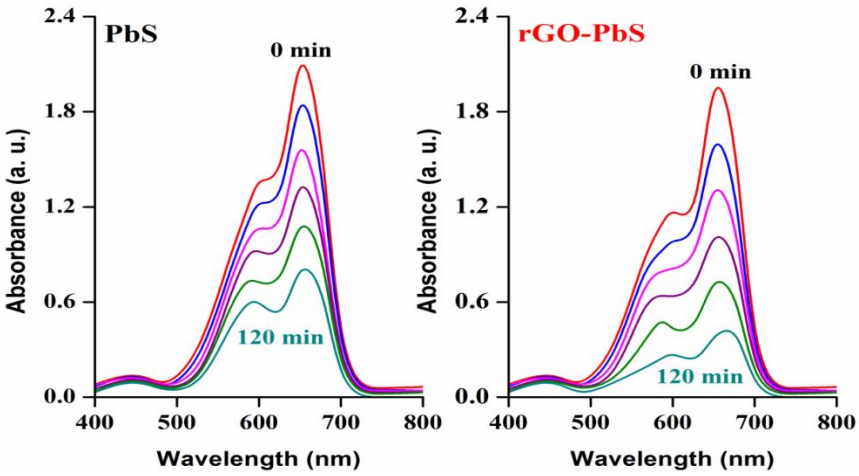

Fig. 6. Degradation profiles of MB in presence of PbS and rGO-PbS. Conditions: MB, 2 mg; temperature, 40 ± 2 °C; total volume, 2 mL).

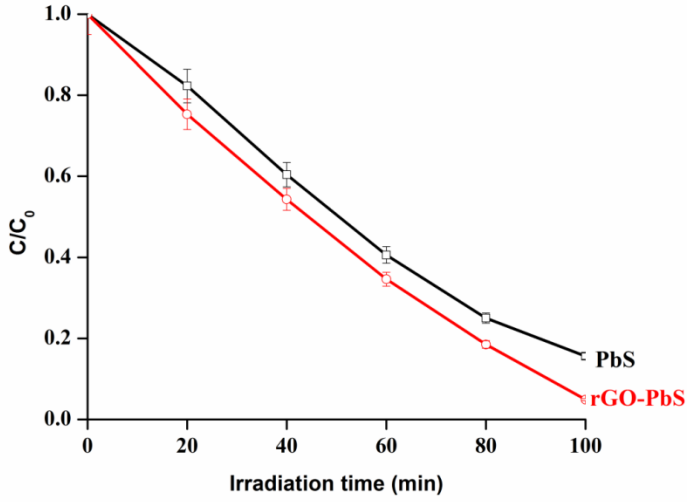

Fig. 7. C/C_o plot of degradation of MB.

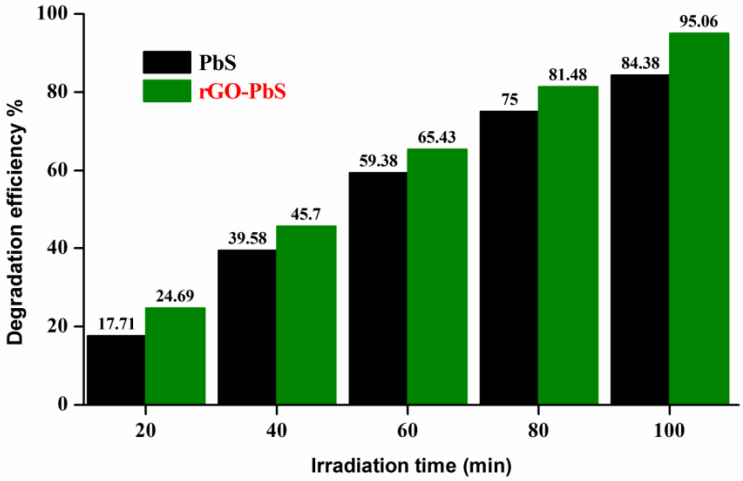

Fig. 8. Bar diagramrepresenting the percent degradation of MB in presence of PbS NPs and rGO-PbS NC.

The factors favoring for the increased photocatalytic activity of rGO-PbS catalyst are: i) rGO offered a larger surface area for the absorption of MB molecules due to its π to π stacking [33], ii) The Fermi levels of rGO sheets are significantly low, hence they could play a vital role in the control of photo-excited electron-hole pairs recombination [34] and iii) heterojunction formed between rGO and PbS facilitates easy electron transfer at the interface [35]. As illustrated in Fig. 9, ln (C/C_0) versus time helped to determine the reaction rate constant. the rate constants using PbS and rGO-PbS NC were 0.0189 and 0.0231 min^{-1}. Because rGO blending created effective charge separation, the rGO-PbS catalyst is exceptionally photocatalytic. Additionally, rGO enhanced the specific surface area for adsorption of MB dye molecules, reducing electron-hole recombination in rGO-PbS catalysts [36].

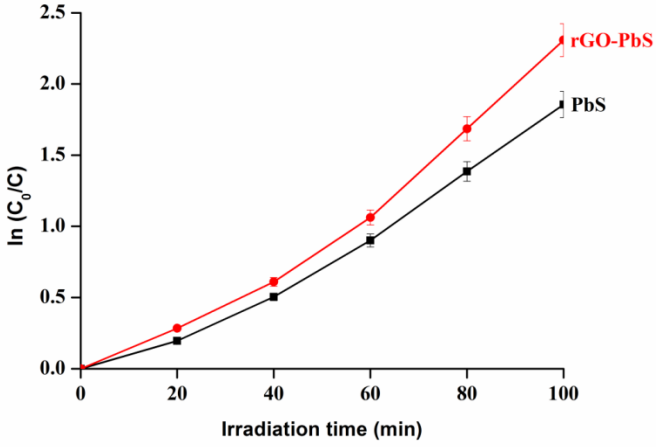

Fig. 9. Kinetic plots for the degradation of MB in presence of PbS and rGO-PbS NC.

The predicted photocatalytic mechanism involved in the PbS and rGO-PbS catalysts (Fig. 10 a,b) is as follows: In dye-photocatalyst (PbS and rGO-PbS) solutions, electrons in the valence band (VB) of PbS are excited to the conduction band (CB) under visible light. The excited e^- reacts with adsorbed O_2 molecules to form O_2^{*-} radicals. OH^- in the aqueous solution takes up VB's h^+ and forms OH^* radicals. In turn, these radicals unfold MB into CO_2 and H_2O by reacting with it. In pure PbS, e^-/h^+ pairs recombine faster, thus slowing down the degradation process. Incorporating rGO sheets to PbS prolonged recombination of e^-/h^+ pairs, resulting in enhanced photodegradation of MB. The rGO sheets in the rGO-PbS catalyst act as a transporter and acceptor of electrons due to their interfacial contact with PbS NPs. Due to this, electrons from the rGO sheets are easily transferred to the CB of PbS, prolonging the recombination of e^-/h^+ pairs, increasing the free carriers in the dye solution containing the rGO-PbS catalyst which further react with O_2 and OH^- present in the mixed solution and form O_2^{*-} and OH^* radicals which effectively degraded MB at relatively higher rate than that of pure PbS NPs.

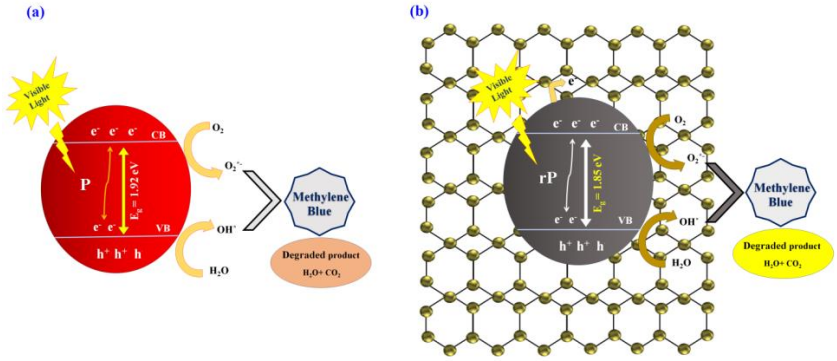

Fig. 10. Photocatalytic mechanism of a) PbS and b) rGO-PbS NC.

Fig. 11 shows the recycle tests performed for the rGO-PbS catalyst. The used rGO-PbS catalyst was extracted from suspension by centrifugation, washed, dried, and its photodegradation ability against MB was evaluated for five cycles. Until the fourth cycle, there was no significant reduction in degradation efficiency. However, the fifth cycle showed a slight reduction in degradation efficiency, which can be attributed to particle aggregation, surface area loss, leaching of the photocatalyst, and a decrease in catalyst amount after washing and drying [37].

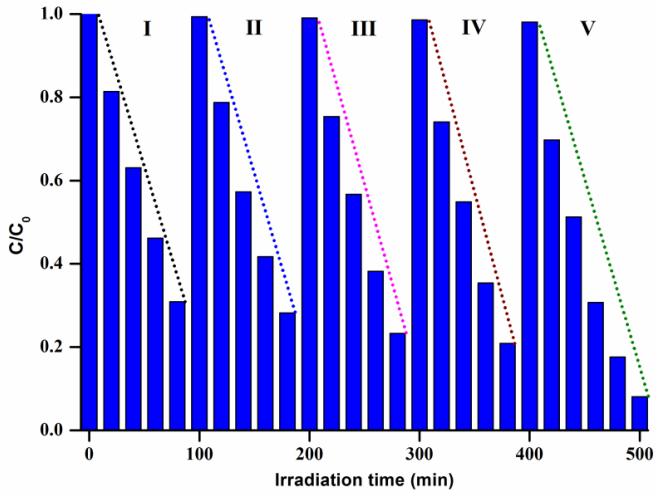

Fig. 11. Recycle tests of rGO-PbS catalyst during degradation of MB.

3.7. *Antibacterial activity*

The antibacterial activities of PbS (P) NPs and rGO-PbS (rP) NC (6 mg dispersed in 20, 40, 60 and 80 µL DMSO) are evaluated against *B. subtilis* bacteria. The inhibition zones developed are shown in Fig. 12 and their values are compiled in Table 1.

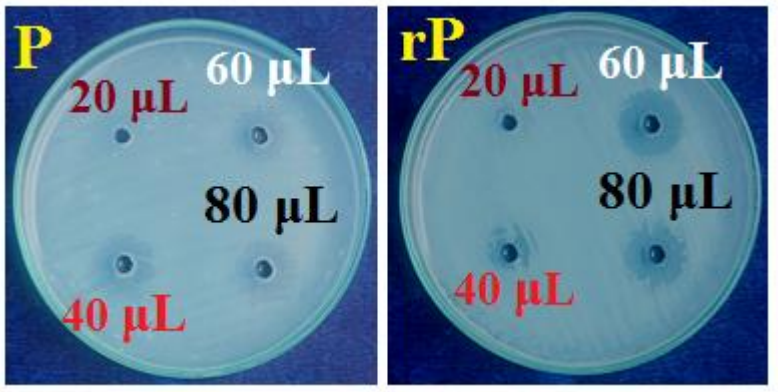

Fig. 12. Digital images of inhibition zones against the presence of PbS (P) NPs and rGO-PbS (rP) NC.

Table 1. Zone of inhibition values developed by PbS and rGO-PbS NPs.

Sample	Zone of inhibition (mm) 6 mg dispersed in DMSO			
	20 µL	40 µL	60 µL	80 µL
PbS	2	8	14	12
rGO-PbS	5	11	24	19

It is seen that rGO-PbS NC exhibited better antibacterial property compared to pure PbS. Both PbS NPs and rGO-PbS NC suppress the pathogen through destroying the cell membrane, impairing deoxyribonucleic acid (DNA) replication, causing oxidative stress via reactive oxygen species, blocking protein synthesis, and interfering with metabolic activity of the bacteria [35]. As a result of their smaller size, the synthesized NPs easily penetrate the cell membrane and bind to proteins, sulfur, oxygen, nitrogen, DNA and phosphorus, resulting in protein denaturation and cell death [38]. The release of metal ions from PbS and rGO-PbS NC, especially Pb^{2+} ions also contribute to their antibacterial activity. Thiol groups (-SH) on the outer surface of proteins attracted to freed metal ions damage the cell membrane by denaturing it [20]. The improved antibacterial activity realized for the rGO-PbS NC can be explained as follows: Upon contact with bacteria, the rGO-PbS NC with a large surface area begins to wrap or adhere to the microbial membrane, in which its hydrophilic moieties, via delocalized conjugated domains, form hydrogen bonds with the bacteria's liposaccharides [39]. Also, with rGO blending, more reactive oxygen species (ROS) were generated for the rGO-PbS NC due to reduced crystallite size which improved its antibacterial potency. The interactive nature of graphene-based nanoparticles appears to enhance their antibacterial activity since they interact directly with genes that code for enzymes and proteins, and both of these processes occur due to DNA intercalation and breakdown [40].

6. Conclusion

PbS NPs and rGO-PbS NC were successfully synthesized by chemical precipitation method. Synthesized particles were examined and compared in terms of their photocatalytic and antibacterial properties. XRD studies confirmed that both samples exhibited cubic crystal structure with decreased crystallite size obtained for the rGO-PbS NC. The rGO-PbS NC exhibited a remarkable degradation efficiency of 95.06 % against MB dye under visible light, with better photo-stable nature. In addition, the rGO-PbS NC is extremely efficient in killing toxic bacterial pathogens. There are a number of factors that account for these good performances, including the uniform deposition of PbS on the rGO sheets and strong interactions between them for efficient charge separation. As a result, rGO-PbS NC has potential applications in the fields of photodegradation and disinfection in the future.

Acknowledgment

XRD studies conducted by Alagappa University are greatly appreciated.

References

1. K. V. Chandekar, T. Alshahrani, A. G. Trabelsi, F. H. Alkallas, M. Shkir, and S. AlFaify, J. Mater. Sci. **56**, 4763 (2021). https://doi.org/10.1007/s10853-020-05539-w
2. A. R. Lara-Canche, V. Vinayakumar, D. F. Garcia–Gutierrez, E. M. Guerra, and D. I. Garcia–Gutierrez, J. Alloys Compnd. **932**, ID 167707 (2023). https://doi.org/10.1016/j.jallcom.2022.167707

3. C. Rajashree and A. R. Balu, Optik **127**, 8892 (2016). https://doi.org/10.1016/j.ijleo.2016.06.106
4. K. Hedayati, D. Ghanbari, M. Kord, and M. Goodarzi, J. Mater. Sci. Mater. Electron. **32**, 373 (2021). https://doi.org/10.1007/s10854-020-04787-5
5. L. N. Maskaeva, V. F. Markov, E. V. Mostovshchikova, V. Voronic, A. V. Pozdin, and S. Santra, J. Alloys compd. **766**, 402 (2018). https://doi.org/10.1016/j.jallcom.2018.06.263
6. Z. R. Khan, and M. Shkir, Physica B **627**, ID 413612 (2022). https://doi.org/10.1016/j.physb.2021.413612
7. K. Szendrei, F. Cordella, M. V. Kovalenko, M. Boeberl, G. Hesser, M. Yarema, D. Jarzab, O. V. Mikhnenko, A. Gocalinska, and M. Saba, Adv. Mater. **21**, 683 (2009). https://doi.org/10.1002/adma.200801752
8. S. Majumder, S. Karade, R. Kumar, M. Gu, B. R. Sankapal, and K. H. Kim, J. Alloys Compd. **906**, ID 164323 (2022). https://doi.org/10.1016/j.jallcom.2022.164323
9. G. Konstantatos and E. H. Sargent, Appl. Phys. Lett. **91**, ID 173505 (2007). https://doi.org/10.1063/1.2800805
10. M. Gu, Y. Wang, F. Yang, K. Lu, Y. Xue, T. Wu, H. Fang, S. Zhou, Y. Zhang, X. Ling, Y. Xu, F. Li, J. Yuan, M. A. Loi, Z. Liu, and W. Ma, J. Mater. Chem. A **7**, 15951 (2019). https://doi.org/10.1039/C9TA02393C
11. M. C. Beard, J. M. Luthe, and A. J. Nozik, Mat. Nanotechnol. **9**, 951 (2014). https://doi.org/10.1038/nnano.2014.292
12. Y. Shao, M. F. El-Dady, L. J. Wang, Q. Zhang, Y. Li, H. Wang, M. F. Mousavi, and R. B. Kaner, Chem. Soc. Rev. **44**, 3639 (2015). https://doi.org/10.1039/C4CS00316K
13. N. Ahmad, S. Sultana, S. Sabir, and M. Z. Khan, J. Photochem. Photobiol. A Chem. **386**, ID 112129 (2020). https://doi.org/10.1016/j.jphotochem.2019.112129
14. A. R. Malik, S. Sharif, F. Shaheen, M. Khalid, Y. Iqbal, A. Faisal, M. H. Aziz, M. Atif, S. Ahmad, M. F. Alam, N. Hossain, H. Ahmad, and T. Botmart, J. Saudi Chem. Soc. **26**, ID 101438 (2022). https://doi.org/10.1016/j.jscs.2022.101438
15 Y. C. Lin, D. C. Tsai, Z. C. Chang, and F. S. Shieu, Appl. Surf. Sci. **440**, 1227 (2018). https://doi.org/10.1016/j.apsusc.2018.01.305
16 C. Rajashree, A. R. Balu, S. C. Devi, C. Kayathiri, K. Devendran, M. Sriramraj, and A. Vinith, Kinetics Catal. **65**, 356 (2024). https://doi.org/10.1134/S0023158423601262
17 A. R. Lara-Canche, V. Vinayakumar, D. F. Garcia-Gutierrez, E. M. Guerra, and D. I. G. Gutierrez, J. Alloys Compd. **932**, ID 167707 (2023). https://doi.org/10.1016/j.jallcom.2022.167707
18. M. Sriramraj, A. R. Balu, S. C. Devi, B. S. Devi, M. Suganya, K. Devendran, M. Karthika, and S. Adityan, Inorg. Chem. Commun. **159**, ID 111734 (2024). https://doi.org/10.1016/j.inoche.2023.111734
19. M. Suganya, A. R. Balu, B. S. Devi, S. C. Devi, M. Karthika, C. Kayathiri, M. Sriramraj, K. Devendran, and S. Adityan, J. Clust. Sci. **35**, 827 (2024). https://doi.org/10.1007/s10876-023-02522-8
20. A. C. Jeoffrey, S. J. Ramalingam, K. Murugaiah, and A. R. Balu, Chem. Phys. Impact **6**, ID 100246 (2023). https://doi.org/10.1016/j.chphi.2023.100246
21. K. Anandalakshmi, P. Venkatachalam, and J. Venugobal, J. Sci. Res. **15**, 1 (2023). https://doi.org/10.3329/jsr.v15i1.56206
22. M. Suganya, A. R. Balu, D. Prabha, S. Anitha, S. Balamurugan, and J. Srivind, J. Mater. Sci. Mater. Electron. **29**, 4312 (2018). https://doi.org/10.1007/s10854-017-8378-0
23. M. Suganya, A. R. Balu, S. Balamurugan, J. Srivind, V. Narasimman, N. Manjula, C. Rajashree, and V. S. Nagarethinam, Surf. Interfaces **13**, 148 (2018). https://doi.org/10.1016/j.surfin.2018.09.005
24. P. Gao, J. Liu, D. D. Sun and W. Ng, J. Hazard. Mater. **250-251**, 412 (2013). https://doi.org/10.1016/j.jhazmat.2013.02.003

25. S. Ravishankar, A. R. Balu, S. Balamurugan, K. Usharani, D. Prabha, M. Suganya, J. Srivind, and V. S. Nagarethinam, J. Mater. Sci. Mater. Electron. **29**, 6051 (2018). https://doi.org/10.1007/s10854-018-8579-1
26. M. P. Abubacker, G. Selvan and A. R. Balu, J. Mater. Sci. Mater. Electron. **28**, 10433 (2017). https://doi.org/10.1007/s10854-017-6815-8
27. N. S. Devi, M. R. Shiekh, L. R. Singh, and A. N. Singh, J. Sci. Res. **16**, 745 (2024). https://doi.org/10.3329/jsr.v16i3.72000
28. S. C. Devi, B. S. Devi, A. R. Balu, K. Devendran, M. Suganya, and M. Sriramraj, Ceram. Int. **49**, 33793 (2023). https://doi.org/10.1016/j.ceramint.2023.08.072
29. S. Ravishankar, A. R. Balu, and V. S. Nagarethinam, J. Mater. Sci. Mater. Electron. **47**, 1271 (2018). https://doi.org/10.1007/s11664-017-5910-1
30. R. Nirmala, K. S. Jeon, R. Navamathavan, H. Y. Kim, and S. J. Park, Mater. Sci. Semicond. Proc. **26**, 575 (2014). https://doi.org/10.1016/j.mssp.2014.05.038
31. K. Rahimi, H. Zafarkish, and A. Yazdani, Mater. Design **144**, 214 (2018). https://doi.org/10.1016/j.matdes.2018.02.030
32. Z. Khan, T. R. Chetia, A. K. Vardhaman, D. Barpuzary, C. V. Sastri, and M. Qureshi, RSC Adv. **2**, 12122 (2012). https://doi.org/10.1039/C2RA21596A
33. J. Bjork, F. Hanke, C. A. Palma, P. Samori, M. Cecchini, and M. Persson, J. Phys. Chem. Lett. **1**, 3407 (2010). https://doi.org/10.1021/jz101360k
34. S. Yousaf, T. Kousar, M. B. Taj, P. O. Agboola, I. Shakir, and M. F. Warsi, Ceram. Int. **45**, 17806 (2019). https://doi.org/10.1016/j.ceramint.2019.05.352
35. P. C. Nethravathi, M. V. Manjula, S. Devaraja, and D. Suresh, Inorg. Chem. Commun. **139**, ID 109327 (2022). https://doi.org/10.1016/j.inoche.2022.109327
36. L. Ma, X. Ai, Y. Lu, S. Yan, and X. S. Wu, J. Alloys Compd. **828**, ID 154406 (2010). https://doi.org/10.1016/j.jallcom.2020.154406
37. A. Irshad, F. Farooq, M. F. Warsi, N. Shaheen, A. Y. Elnaggar, E. E. Hussein, Z. M. El-Bahy, and M. Shahid, Flatchem **31**, ID 100325 (2022). https://doi.org/10.1016/j.flatc.2021.100325
38. L. Juan, Z. Zhimin, M. Anchun, L. Lei, and Z. Jingchao, Int. J. Nanomed. **5**, 261 (2010). https://doi.org/10.2147/IJN.S8810
39. R. Lv, Y. Q. Liang, Z. Y. Li, S. L. Zhu, Z. D. Cui, and S. L. Wu, Rare Met. **41**, 639 (2022). https://doi.org/10.1007/s12598-021-01759-4
40. Y. Liu, Y. Luo, J. Wu, Y. Wang, X. Yang R. Yang, B. Wang, J. Yang, and N. Zhang, Sci. Rep. **3**, 2975 (2013). https://doi.org/10.1038/srep02975